J Nanopart Res (2020) 22:78
https://doi.org/10.1007/s11051-020-04792-z

RESEARCH PAPER

Fabrication of double-sided comb-like F/Ce co-doped $BiVO_4$ micro/nanostructures for enhanced photocatalytic degradation and water oxidation

Hayder A. Abbood · Akram Alabdie · Adnan Al-Hawash · Anwar A. Abbood · Kaixun Huang

Received: 12 November 2019 / Accepted: 24 February 2020

Abstract Hierarchically branched structures have attracted particular attention for the application in photocatalysis owing to their special physicochemical features. But the construction of hierarchical branch semiconductors is usually expensive and complex. In this work, a novel double-sided comb-like fluoride (F^-) and cerium (Ce^{3+}) co-doped monoclinic $BiVO_4$ macro/nanostructured photocatalyst (BFCe) was successfully prepared through coupling via a facile hydrothermal method and calcination at 500 °C. A possible growth mechanism of the double-sided comb-like monoclinic $BiVO_4$ was proposed and discussed. Compared with undoped (BVO) and F (BF) and Ce (BCe) single-doped bismuth vanadate, the BFCe sample (the mass ratio of Ce^{3+} to F^- was 1:2) exhibited considerably increased photocatalytic performance toward degrading the rhodamine blue dye (94.8%) and water splitting (O_2 evolution was 338.59 μmol/g). Experimental results showed that the F^- and Ce^{3+} doping expands the visible light absorbance while enhancing the specific surface area. Thus, the double doping of F^- and Ce^{3+} provided a synergistic effect, resulting in optimized photocatalytic decomposition efficiency, as corroborated by luminescence spectroscopy measurements. This work can serve as a useful guide for the engineering design of novel micro/nanomaterial with an increased catalytic performance for various applications.

Keywords Micro/nanostructure · $BiVO_4$ · Co-doping photocatalysis · Photodegradation of dyes

Electronic supplementary material The online version of this article (https://doi.org/10.1007/s11051-020-04792-z) contains supplementary material, which is available to authorized users.

H. A. Abbood (✉) · K. Huang
School of Chemistry and Chemical Engineering, Huazhong University of Science and Technology, Wuhan 430074, People's Republic of China
e-mail: hayder.abood@uobasrah.edu.iq

H. A. Abbood
Department of Material Engineering, College of Engineering, University of Basrah, Basrah, Iraq

A. Alabdie
South Refineries Company, Ministry of Oil, Basra 61006, Iraq

A. Al-Hawash
Department of Chemistry and Environmental Science, Marine Science Centre, University of Basrah, Basrah, Iraq

A. A. Abbood
Department of Chemical Engineering, College of Engineering, University of Basrah, Basrah, Iraq

Introduction

The increased interest in the area of photocatalysis during the past decade has led to an intensified study on the so-called traditional semiconductor materials (Park et al. 2013). Photocatalysis uses visible light illumination to produce photoexcited carriers in the photocatalysts. After that, the excited carriers, i.e. holes (h^+) and electrons (e^-), pass to the surface of the photocatalyst for oxidative and reductive reactions, respectively (Hoffmann

Published online: 24 March 2020

et al. 1995). The photodegradation of organic contamination and O_2 evolution is especially needed to utilize the active semiconductors in visible light as renewable sources (Huang et al. 2014). Among many photocatalyst candidates, $BiVO_4$ may be the most promising (Wang et al. 2012). The $BiVO_4$ photocatalysts for visible oxidation was first reported by Kudo et al. (1998). Subsequently, considerable effort has been given to understand the nature of the monoclinic $BiVO_4$ (energy gap of about 2.4) responsible for the restricted intrinsic catalytic properties (Walsh et al. 2009; Regmi et al. 2019). Determining this nature may be possible through detailed experimental and theoretical studies on the mobility and collection of photogenerated charge carriers (Saison et al. 2015), transport charges to catalytic sites (Mohamed et al. 2019), improper position of the conduction band (Meng and Zhang 2016) and poor light adsorption abilities; all of which have been associated with the structure of monoclinic $BiVO_4$ (Lin et al. 2017). A variety of choices (such as controlling the size (Xu et al. 2018), surface modification (Pi et al. 2014), novel nanostructures (Jaihindh et al. 2019), heterojunction structures (Lopes et al. 2016) and porosity (Kim and Choi 2014)) have been proposed to overcome the undesirable recombination of (e^-) and (h^+) and complete the conduction band position requirements (Tan et al. 2017). To date, design of $BiVO_4$ hierarchical structures is another functional choice to develop photocatalytic degradation performance (Hu et al. 2019; Takashima et al. 2019). The tailoring of novel topologies, such as dendritic, comb-like, saw, star, rings, tubes and hyper-branching, exhibits multiple advantages (Abbood et al. 2013) such as increased active sites, rate relocation of reactant molecules and increased efficiency of incident light capture (Wang et al. 2016).

Consequently, a flexible, easy, low cost and environmentally friendly strategy to improve the photoresponsive efficiency of $BiVO_4$ has been found through doping with suitable ions/atoms (Chen et al. 2019; Obregón and Colón 2014; Pattengale and Huang 2016; Saithathul Fathimah et al. 2014; Wang et al. 2017). The doping ions/atoms have replaced either the Bi(I) or V(II) atoms but little attention has been paid to replace the O(III) site of $BiVO_4$ (Ullah et al. 2018). Based on a previous work (Yin et al. 2013), desired changes are considered expedient due to the fluctuations in band gaps and increasing e^- or h^+ densities after inserting the dopant into the regular lattice of $BiVO_4$ (Zhao et al. 2010). Indeed, an actual correlation exists among the dopant valence state, place in the lattice, and amount of solid-state solution (Usai et al. 2013). Furthermore, the difference in the atomic size of the host and dopant states in the lattice is dissimilar with the corresponding oxides of metals, as manifested by the solubility level in a host structure (Geng et al. 2015). In this context, Li et al. (2013) revealed an increased number of oxygen vacancies resulting from the exchange of an O atom-doped F^- ion to build an F–V–O system in the crystal lattice of bismuth vanadate. The photocatalytic properties of $BiVO_4$ in the visible zone can be further tuned by the alignment and synergistic effects of metal ion/non-metals as a co-dopant (Zheng et al. 2016). For example, a higher photoactivity toward the degradation of methyl orange has been reported by Wang et al. (2013a) after introducing optimal concentrations of Eu, B in $BiVO_4$. The synergy between B and Eu under visible light contributes to increased oxygen vacancies, reduction in the band gap and creation of a higher specific area. Wang et al. (2013b) reported La and B-co-doped $BiVO_4$ and demonstrated that La(III) inhibits the recombination of photogenerated electrons. Zhengs group (Wang et al. 2015) used the sol-gel method to synthesize the N and Sm couple-doped $BiVO_4$. The absorption in the visible zone and photoactivity of N and Sm addition are clearly enhanced due to the combined behaviours of the co-dopants. Xue et al. (2017) ascribed the superior photoactivity of Eu and F couple-doped $BiVO_4$ microspheres to the synergistic effect of the Eu and F co-doping. Finally, the effects of S and W co-doping on the photoactivity of $BiVO_4$ have been studied by Regmi et al. in detail (2018).

Based on literature (Wang et al. 2014; Gu et al. 2015; Jiang et al. 2016; Luo et al. 2017), the F^- and Ce^{3+} ions can improve photocatalytic efficiency if they are properly co-doped in the monoclinic $BiVO_4$ lattice. Herein, a unique double-sided comb-like F/Ce co-doped $BiVO_4$ composed of microrods and nanosheets was constructed via simple hydrothermal process assisted with calcinations. A time-dependent study was also carried out to explore the growth and possible mechanism of the products. Significantly, the BFCe exhibits higher photocatalytic activities than the other prepared samples for both water decomposing and dye degradation. Additionally, we explored the roles of Ce^{+3} and F^- dopants and have discussed the reactive species-trapping tests in order to gain an in-depth knowledge on the increased photocatalytic performance.

Materials and methods

Materials

All chemical reagents are of analytical grade and were purchased from Beijing Chemicals Co., Ltd., and used as received without further purification.

Preparation of photocatalysts

$BiVO_4$ was fabricated by a simple hydrothermal route. Bi $(NO_3)_3.5H_2O$ (1.5522 g, 3.199 mmol) and EDTA (1.305 g, 4.465 mmol) were dissolved in 15-mL deionized (DI) water, forming a cheated Bi complex labelled as solution A. In another beaker, (0.3743 g, 3.199 mmol) NH_4VO_3 was dispersed in 15 mL (DI), and this solution was labelled as solution B. Under vigorous mixing for several minutes, solution B was gradually added into solution A. Subsequently, the pH of the mixture was adjusted to 10 with aqueous 10% NaOH. The colour of the precipitate slowly changed to yellow. Then, a certain amount of $Ce(NO_3)_3.6H_2O$ and (0.031 g, 0.738 mmol) NaF was added to the mixture. To prepare different samples, the mass ratio of Ce^{3+} to F^- was adjusted to 0.7, 1.2 and 2.1, respectively. Finally, the mixture was poured into a 40-mL Teflon-lined stainless steel autoclave, sealed tightly and kept at 180 °C for 12 h. The autoclave was cooled naturally, and the double comb-like structure powders were collected, washed with water and anhydrous ethanol several times and dried at 70 °C for 12 h. The obtained product was heated at 400 °C for 1 h. The co-doping sample was labelled as BFCe, the single dopant by Ce^{3+} was labelled as BCe, the single dopant by F^- was labelled as BF, and pristine $BiVO_4$ was labelled as BVO. The final composition (wt%) of Ce^{3+} and F^- in bismuth vanadate was determined by XPS.

Characterization techniques

X-ray diffraction (XRD) patterns were detected by an X-ray diffractometer (Panalytical X'Pert Pro; Netherlands) with Cu Ka ($\lambda = 0.15418$ nm), at an angular 2θ and speed of 2° per minute. The Brunauer-Emmett-Teller (BET) of the samples was determined on a Micromeritics ASAP 2020M Surface Area and Porosity Analyzer. The as-prepared sample was degassed at 110 °C for 8 h under vacuum (10^{-5} bars). Surface morphologies of synthesized samples were performed by field emission scanning electron microscopy (FE-SEM) (SIRION 200). Raman spectrometer (HR 800, LabRam, Horiba) with a 532.15-nm excitation wavelength and X-ray photoelectron spectrometer (XPS-AXIS-ULTRA DLD high-performance imaging, Shimadzu, Japan) were used to analyse the functional groups on the surface and the chemical composition of these materials. Photoluminescence (PL) tests were performed on a (FLS980, Edinburg Instruments, UK) spectrophotometer fitted with a photomultiplier tube (PMT) detector (Hamamatsu). The excitation source was a standard 450 W Xenon lamp. The nitrogen adsorption-desorption isotherms were carried out with an ASAP 2020 adsorption apparatus (Micromeritics Instrument Co., USA).

Photocatalytic activity

Photo-oxidation of water

The photocatalytic oxidation activity of the prepared Ce-$BiVO_4$ powder samples was performed in 100 mL of $AgNO_3$ (00.1 M) solution under UV−vis light from a 250-W mercury lamp, GYZ 220–230 V, Philips Electronics coupled with a cut-off filter L42. A total of 50 mg of the as-photocatalyst was suspended into the $AgNO_3$ solution kept at room temperature in a gas-closed-circulation system; subsequently, the system was sealed, and purged with carrier gas N_2 for 30 min to remove the residual oxygen. The amount of O_2 production was assessed by gas chromatography using a thermal conductivity detector (GC7890II, Tianmei, Shanghai; nitrogen carrier gas). The irradiance of the lamp just above the solution has been measured, and the visible light intensity was about 0.8846 MW/cm^2.

Photocatalytic degradation

The photodegradation of activity of a rhodamine blue solution (RhB, $\lambda_{max} = 554$ nm) was determined in a three-neck glass reactor (250 mL) equipped with a reflux condenser and air diffusion. The fixed as-prepared powder (50 mg) was dispersed in a RhB (10 mg L^{-1} in 200 mL) aqueous solution, followed by at least 30 min stirring in the absence of light in order to achieve adsorption–desorption equilibrium of RhB on the photocatalyst surface. The suspension was then expose to visible light irradiation by a 250-W (GYZ 220–230) mercury lamp, Philips Electronics (filter to cut off light less than $\lambda = 420$ nm). The light intensity applied to the photoreaction vessel was approximately 0.8846 MW/

cm^2 for 100 min. A series of 5-mL samples were taken every 20 min and separated from the suspended catalyst particles for spectrophotometric monitoring (Shimadzu, model No. 2450s) analysis.

Result and discussion

XRD and crystal analysis

Figure 1 displays the X-ray patterns of the as-synthesized samples that underwent hydrothermal process and calcination at 500 °C. All the reflection peaks of undoped (BVO), F (BF), Ce (BCe) single-doped bismuth vanadate and the co-dopant BFCe products can be indexed to a monoclinic-scheelite $BiVO_4$ (JCPD No: 14-0688). Moreover, the BVO favoured the growth along the (040) direction, whereas co-doping with F/Ce and doping with F^- or Ce^{3+} seemed to have an opposite effect. A gradual slight shift in peak (121) toward the left (lower angle) was observed with doping by F−, Ce^{3+} and F^-/Ce^{3+} co-doping, thereby suggesting the effective incorporation of the dopant to change the local environmental structure of monoclinic-scheelite bismuth vanadate. No characteristic peaks for Ce^{3+} or F^- or their oxide species indicated the substitution of Ce^{3+} and F^- in the $BiVO_4$ crystal lattice rather than the constitution of other phases. Furthermore, the single doping or co-doping of Ce^{3+} and F^- did not change most of the pattern positions nor induce the transition of the monoclinic phase to the tetragonal structure. The key factor to stabilize the monoclinic structure was the ability to replace O^{2-} with F^- under similar oxidation state and match the ionic radius of Ce^{3+} and Bi^{3+}. The 121 plane for monoclinic $BiVO_4$ was selected to calculate the average crystallite size (D) and lattice distortion (ε) by using the Scherrer equation: $D = 0.9\lambda/(\beta\cos\theta)$ and $\varepsilon = (\Delta d/d)\% = (\beta/4\tan\theta)\%$. The variation in crystal sizes due to single doping and co-doping is listed in Table 1. The F− doping slightly increased the ε, which can suppress the recombination of e^-–h^+ pairs. The D decreased in the BF sample, which can be attributed directly to substitution of lattice O^{2-} to F^-. However, Ce doping clearly increased the D.

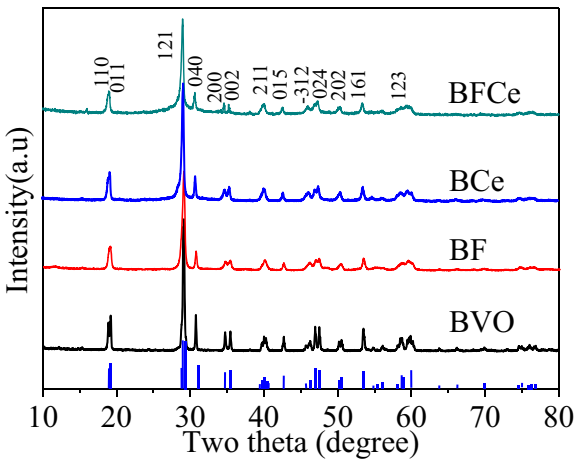

Fig. 1 X-ray diffraction patterns of fabricated samples

FE-SEM analysis

Figure 2 illustrates the FE-SEM images of the BFCe powder prepared at a temperature of 210 °C and reaction time of 12 h. The sample contained several 3D BFCe micro/nanostructures with an average size of about 2 μm, suggesting that high yield and acceptable uniformity can be readily attained by this strategy (Fig. 2a, b). The magnified FE-SEM image in Fig. 2c and d clearly indicates that each side of the 2D nanosheets represented unevenly distributed microrod arrays. The majority of this sample showed morphology just like the structure of the double-sided comb assembled by BFCe microrods and 2D BFCe nanosheets. The microrod array grew perpendicularly on both surfaces of the nanosheets. The average thickness, width and length of the nanosheets were approximately 50, 300 and 800 nm, respectively. The average diameter and length of the BFCe microrods were approximately 200 nm and 1.2 μm, respectively. The FE-SEM images of the BVO, BF and BFCe samples are shown in Fig. SI (Supplementary Information).

XPS analysis

The chemical composition and local electronic environment of the pure, doped and co-doped double-sided comb-like $BiVO_4$ micro/nanostructures were analysed by XPS. The overall scan spectrum shown in Fig. 3a revealed the existence of O, V, Bi and C elements in the BVO, whereas F^- and Ce^{3+} were observed in the doped and co-doped powders. The results for the binding energies were adjusted on the basis of the C1s value of 284.6 eV. As shown in Fig. 3b, two strong symmetric peaks cantered at binding energies of 158.7 and 164 eV were generally assigned to the spin-orbit splitting of Bi $4f_{7/2}$ and Bi $4f_{5/2}$, respectively (Liu et al. 2017b). The slight shifting of peaks in the BF, BCe and BFCe samples

Table 1 Average crystallite size, band structure-specific surface areas (BET) and rate constant of the fabricated samples

Sample	Crystal size	ε%	Eg (eV)	E_{VB} (eV)	E_{CB} (eV)	Surface area BET (m^2/g)	Rate const. (k in min^{-1})
BVO	23.67	15.85	2.29	2.268	0.42	29.87	0.00077
BF	19.13	18.36	2.23	2.66	0.43	32.00	0.00105
BCe	28.9	21.73	2.16	2.62	0.46	33.75	0.00158
BFCe	30.64	22.54	2.08	2.58	0.5	42.15	0.00311

may be caused by the different electro-negativities and strong interaction of dopants F^- and Ce^{3+} with O, V and Bi (Kong et al. 2019; Zhang et al. 2019).

The F1s X-ray photoelectron spectra for the BF and BFCe samples are presented in Fig. 3c. The peaks of F1s were at 683.98 and 684.26 eV for the BF and BFCe products, respectively, which can be ascribed to the F^- substituting the O^{2-} in the lattice of bismuth vanadate to create an F–V–O system (Li et al. 2013). Moreover, the higher electronegativity of F^- than O^{2-} and replacing Bi^{3+} with Ce^{3+} increased the transfer of more electrons to the F^- and/or reduced the electron density of the vanadium atoms. Thus, a comparatively higher binding energy (684.26 eV) for BF than for V-F and/or Bi-F was found in BFCe (the F1s binding energy was 683.98 eV). These results suggested that the F^- dopant easily exchanged the O in the bismuth vanadate crystal structure via hydrothermal processes without absorbing F on the vanadium and/or bismuth in the BF and BFCe products. This suggestion was also supported by the unchanged position of the diffraction peak in the XRD outcomes.

The XPS signals of the Ce^{3+} $3d_{5/2}$ and $3d_{3/2}$ ions can be fitted into two sets of two Gaussian peaks at 872.16 and 879.91 eV; 886.54 and 889.33 eV for BCe; and 870.99, 874.66, 888.08 and 892.03 eV for BFCe (Fig. 3d). No peaks corresponding to the Ce^{4+} 4f states and any Ce species were observed during the X-ray analysis. The binding energy value for Ce^{3+} was smaller than the one achieved previously (Luo et al. 2017), indicating that the occurrence of F^- in the crystal lattice seriously affected the electronic structure environment. These results suggest that the addition of Ce^{3+} can be incorporated into the lattice of bismuth vanadate via the hydrothermal route.

The asymmetric profiles of the V 2p3/2 in Fig. 3e indicated two peaks for each sample, that is 516.27 and 517.01 eV for BVO, 516.31 and 516.97 eV for BCe, 516.50 and 517.13 eV for BF and 516.58 and 517.27 eV for BFCe, thereby demonstrating the V^{4+} (as minor) and V^{5+} (as major) species (Regmi et al. 2017). By contrast, the appearance of the V^{4+} peak may be caused by the substitution of Ce^{3+} instead of Bi^{3+} in the crystal lattice. The V^{4+}/V^{5+} molar ratios on the surface region of BVO, BCe, BF and BFCe were 0.098, 0.19, 0.28 and 0.42, respectively, as estimated by the XPS. An increase in the V^{4+}/V^{5+} ratio favoured photocatalysis, where V^{4+} distorted the VO_4 tetrahedron structure and behaved as h^+ and trap e^- by altering the photoexcited e^-–h^+ pairs' recombination on the photocatalyst surface (Wang et al. 2017).

Fig. 3f shows the XPS spectra of O1s for the BVO, BF, BCe and BFCe products. The BVO showed a signal centred in the 530.07-eV region. Each asymmetrical broad peak for the BF, BCe and BFCe products illustrated two signals. The stronger signal was found in the lattice oxygen (O_{latt}) at 529.83–530.12 eV, while the weaker signal at a binding energy of 530.94–531.79 eV is for adsorbed oxygen (O_{ads}) species (Li et al. 2017). The molar ratios of O_{ads} to O_{latt} at the surface were 0.11 for BVO, 0.36 for BF, 0.25 for BCe and 0.39 for BFCe. The quantity of chemisorbed oxygen in the BFCe sample was higher than that in the undoped BVO, BF and BCe samples, suggesting that the creation of oxygen vacancies was due to co-doping. Photoinduced electrons were also captured through the assistance of defects, which resulted in double doping, of which the recombination of h^+ and e^- production was severely limited. The hydroxyl group (OH^-) and adsorbed water on the surface of the photocatalyst were able to react with the h^+ during photocatalysis to form (•OH) radicals, which were responsible for the decomposition of organic effluents. As shown in Table S1, the BFCe sample possessed higher amounts of surface V^{+4} and O_{ads} species than the BVO, BiF and BCe samples due to the coexistence of F^- and Ce^{3+} (Park et al. 2011).

Raman analysis

Fig. S2 displays the Raman curve of the samples derived from calcination at 500 °C. The spectra of the BVO, BF,

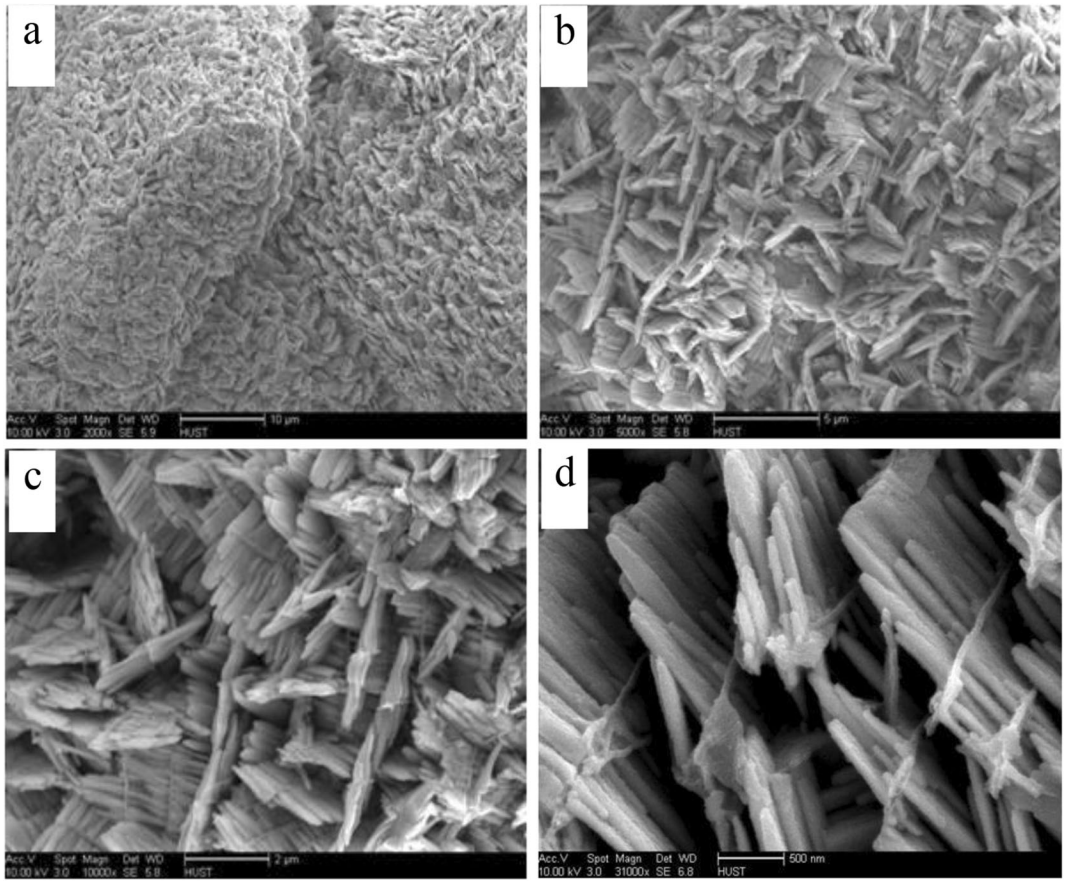

Fig. 2 (**a**, **b**) and (**c**, **d**) presented the low and high-magnification FESEM images of BFCe sample

BCe and BFCe samples illustrated absorptions at 829.72, 317.62, 360.87 and 201.60 cm^{-1}, respectively, which were ascribed to the symmetric bending, symmetric stretching and asymmetric bending modes, respectively, of VO_4^{-3}. No shifts in the main Raman bands led to the conclusion that the Ce atoms did not replace V in the crystal system, which was in agreement with the result of previous literature (Gu et al. 2016). The purity of BVO, BF, BCe and BFCe can be unambiguously ensured as no other ascended peaks were apparent in the Raman charts. These results suggested an improved monoclinic structure of $BiVO_4$ in the as-prepared powders and XRD findings.

Optical property analysis

The optical absorption spectra of BF, BCe and BFCe photocatalysts in comparison with BVO are displayed in Fig. 4a. The wavelength of absorption obtained for all samples was more than 500 nm, suggesting strong absorption in the visible zone and the monoclinic phase of $BiVO_4$. The absorption signals of the products were altered in a systematic manner. Different dopants normally induce dissimilar band gaps. The red shift trend is a reliable method to determine the transition band gap energy as calculated by the Kubelka-Munk formula shown in Eq. (1).

$$(\alpha h\nu)^n = \mathrm{A}\left(h\nu - E_g\right) \tag{1}$$

where $h\nu$, α and E_g are the photon energy, absorption coefficient and band gap energy (eV), respectively, and the constant A is equal to one (Xiao et al. 2017). Given that $BiVO_4$ is classified as a direct semiconductor, the value of n is 2. The band gaps were estimated on the basis of linear part of the $(\alpha h\upsilon)^{2-}$ versus hυ plot, as illustrated in the inset of Fig. 4a. Table 1 shows that the hybridization of the orbital's O2p, F1s and Bi6s and disturbance in the valence band (Wang et al. 2014) resulted in the band gap of BF at 2.23 eV, which was

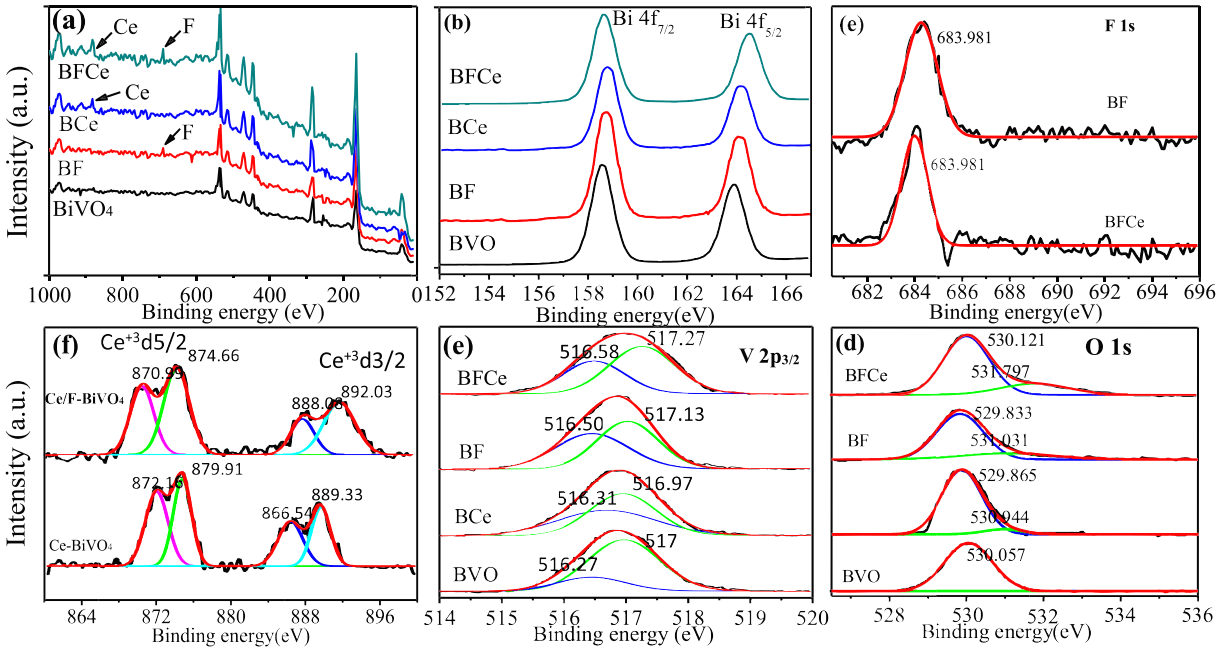

Fig. 3 XPS spectra of the synthesized samples. **a** Survey spectrum of BVO, BF, BCe and BFCe. **b** High-resolution Bi4f spectra of BVO, BF, BCe and BFCe. **c** F1s peak of BF and BFCe. **d** High-resolution deconvoluted Ce 3D spectra of BCe, and BFCe. **e**, **f** High-resolution V2p and O1s spectra for BVO, BF, BCe and BFCe, respectively

lower than that of BVO at 2.29 eV. The lattice deformation and formed vacancy occurred when Ce^{3+} was introduced, leading to the band gap of BCe being reduced further to 2.21 eV. Consequently, the F^- and Ce^{3+} co-dopants can synergistically be responsible for the enhanced photoactivity, because the reduction in the band gap of BFCe to 2.08 eV increased the separation rate of photogeneration e^-–h^+ pairs.

As shown in Table 1, the position of the band edge of the BFCe powder was estimated using the equation $E_{VB} = \chi - E_o + 0.5E_g$, where E_g, E_o, E_{VB} and χ are the measured band gap, free electron energy in hydrogen scale (~ 4.5 eV), potential valence band tail and electronegativity (6.04 for bulk $BiVO_4$), respectively (He et al. 2018). Similarly, the equation $E_{CB} = E_{VB} - E_g$ was employed to determine the conduction band E_{CB} position (Abbood and Huang 2018), and the values are listed in Table 1.

Generally, the couple doping of F^- and Ce^{3+} leads to a reduction in the band gap through the intermixing of hybridized O2p and Bi6s with the F1s in the valence band of the as-prepared bismuth vanadate. The higher valence electrons of Ce^{3+} atoms than those of Bi or V atoms supplied excess electrons that encouraged the rise in Fermi energy level with the generation of an in-gap situation between the conduction and valence bands. This level of in-gap energy assisted in the successive photoexcitation from the highest valence band to the bottom of the conduction band under visible light illumination, thereby loading easy charge transfer. Hence, the synergetic effect of couple dopants F^- and Ce^{3+} enhanced the absorption efficiency, which subsequently improved the photoactivity of the BFCe sample.

Photoluminescence spectroscopy

The PL spectra are suitable for investigating the transfer, migration and separation efficiency of the e^-–h^+ pairs in the prepared photocatalysts (Liu et al. 2017a). As shown in Fig. 4b, the BF, BCe, BFCe and BVO samples displayed broad emission spectra in the range of 510–580 nm centred at approximately 530 nm at an excitation wavelength of 335 nm. However, the signal intensity for the single and co-doped samples showed a remarkable drop compared with vanadate BVO. The intense emission from BVO can be attributed to the intrinsic luminescence because of the recombination between the e^- in the conduction band and h^+ in the valence band. The decrease in the PL intensity of the BFCe sample was a solid indication of the enhanced e^-–h^+ separation efficiency in the surface of the sample as a result of doping. This result led to the smallest recombination rate of e^-–h^+ pairs in the BFCe product under

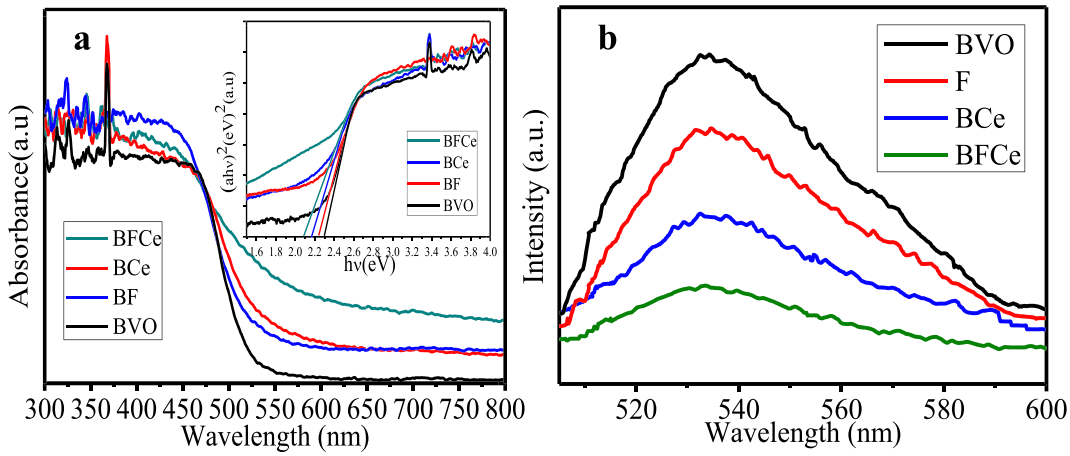

Fig. 4 **a** UV-Vis DRS spectra of the synthesised sample, inserted plots of $(ahn)^2$ versus hn for the band gap energy. **b** Room temperature PL spectra of the samples

visible light illumination and high photoactivity that coincided with the subsequent increase in photodegradation of RhB.

Formation mechanism

The growth of double-sided comb structures can be understood on the basis of metal oxide seed thickness (Fig. S3). Many models have been promoted to explain the formation of inorganic comb-like nanostructure (Lao et al. 2004; Tian et al. 2006). A similar process was suggested by Li et al. (2016) for the synthesis of 3D double-sided comb-like ZnO on Si substrate seed thickness. These growth mechanisms can be used to explain the formation of the proposed BFCe. In this regard, the time-dependent morphological evolution of the intermediate formation was performed at various time intervals of 3, 6, 9 and 12 h in the hydrothermal process followed by calcination at 500 °C for 1 h. The FE-SEM images of the different intermediate products clearly revealed the growth process (Fig. S3). At the early reaction stage, no precipitate appeared before two and a half hours. After 3 h, irregular nanoparticles were produced, as shown in (Fig. S3a). Nanosheet arrays were obtained at 6 h, but the surface of the nanosheets was almost smooth (Fig. S3b). After 9 h, nanoparticles with different diameters can be clearly observed on the double-sided nanosheets surfaces (Fig. S3c). Upon prolonging the reaction time to 9 h, nanoparticles grew on the double-sided nanosheets, and their growth fronts were not similar. This finding suggested commonality in the growth process. After 12 h of hydrothermal reaction, the microrod density and length of the two surfaces of the nanosheets increased (Fig. S3d) which was an evidence of different growth modes. This observation excluded the possibility of the dendrite morphology formation of the powder. A schematic of the BFCe is summarized in Fig. S4.

O_2 evolution through water splitting

Figure 5 shows the photocatalytic water oxidation activities of BVO, BF, BCe and BFCe samples in a mixture containing silver nitrate (0.1 M) as an electron scavenger under visible light illumination. The BVO exhibited low photocatalytic water oxidation activity (82.97 μmol g^{-1}). As F^- and Ce^{3+} were incorporated, the photoactivities of O_2 generation reaction progressively increased to 142.55 and 181.29 μmol g^{-1} for the BF and BCe samples, respectively. The highest photocatalytic activity of 338.59 μmol g^{-1} represented an increase in a factor of 4 obtained from the co-doped sample BFCe compared with BVO. The O_2 evolution ceased after 100 min (Fig. 5) due to silver cluster deposition on the reactor walls that prevented the visible light coming from the outside of the reaction vessel. Indeed, this limitation was previously highlighted by Wang et al. (2019). Thus, the improved photocatalytic O_2 activity was a consequence of the charge separation at the BFCe surface.

Photodegradation of RhB

The photocatalytic activities of the as-prepared photocatalysts were detected using the optical

absorption at 554 nm of the RhB solution under visible light irradiation. Results showed the minimal adsorption of the RhB dye on BFCe surfaces and no tendency to catalysed dark reactions to the surface of the samples. Furthermore, the direct photolysis of RhB via visible light illumination (Fig. 6a) was unimportant. These results suggest that photocatalytic conversion was responsible for removing RhB. A remarkable enhancement in the decomposition of RhB was detected in the presence of the as-prepared samples (Fig. 6a).

Under visible light illumination, the photocatalytic degradation efficiencies of RhB on the as-prepared BVO, BF, BCe and BFCe products were 37.9%, 68.213%, 66.7% and 94.8%, respectively, at 100 min. The highest decomposition rate was found on co-doped BFCe. The absorbance curve of BFCe illustrated the disappearance of signals in the region of $\lambda < 400$ nm (inset of Fig. 5a), which can be ascribed to the degradation of the phenyl ring of RhB. The effect of $Ce3^{+}$ concentration on the degradation of RdB was also studied (Fig. S5).

Circulating tests on the photodegradation of the RhB dye under visible light were applied to verify the photocatalytic stability of the BFCe sample (Fig. 6b). After the three recycling of the photodecomposed of RhB dye, the photoactivity of this sample slightly decreased, indicated that the BFCe has good photostability, which is particularly important for the practical application of BFCe.

Given that the RhB dye can absorb light in the visible region, a number of mechanisms can be proposed for its photodegradation by BFCe. (1) The direct photolysis of RhB is typically very slow and impractical because of the tools used to remove the RhB dye from waste water. (2) The RhB photoanodic or photocathodic sensitization (i.e. charge injection from a photoexcited dye leaving unstable RhB dye $RhB^{-\bullet}/RhB^{+\bullet}$), and the injected charges, may form other radicals. (3) In the photocatalytic oxidation process, generally, the organic materials are attacked by photogenerated active species, including hydroxyl radical ($^{\bullet}OH$), h^{+} and/or superoxide anion radical ($^{\bullet}O_2^{-}$) scavengers (Yang et al. 2019; Yu et al. 2019). Thus, the photodegradation depends on the adsorption of the RhB dye, OH^{-}, H^{+}, O_2 and/or H_2O on the surface of BFCe. Tert-butyl alcohol (TBA), benzoquinone (BQ) and ethylenediaminetetraacetic acid (EDTA) were added to photoreaction system as the scavengers of $^{\bullet}OH$, $^{\bullet}O_2^{-}$ and h^{+}, respectively, to determine the mechanism of photodegradation and further explore the relationship among the function of these radicals in the photodegradation process (Fig. 6c).When BQ was added, the decomposition rate of RhB dye decreases slightly, and there was no obvious modification when TBA is added. However, the decomposition rate is decreased considerably with EDTA addition. Thus, h^{+} is the dominant active radical in the photodegradation followed by $\bullet O_2^{-}$, whereas the •OH radical contributed little to the photodegradation process with BFCe. The RhB dye was degraded by the participation of h^{+}, $\bullet O_2^{-}$ and $^{\bullet}OH$ in small fragments.

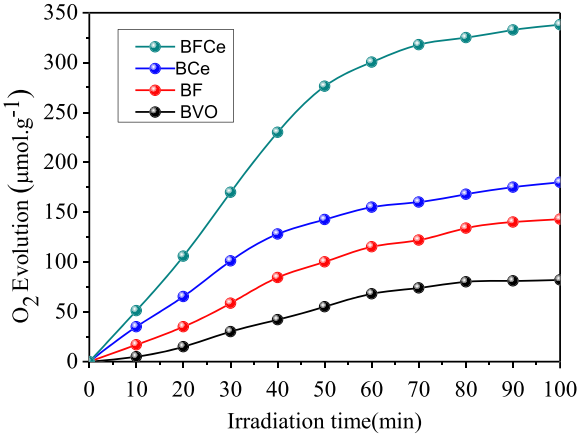

Fig. 5 Photocatalytic O_2 evolution for samples under UV–vis light irradiation

The pseudo-first order reaction equation was successfully applied to calculate the kinetics reaction constants and further investigate the mechanism (Abbood et al. 2012). Figure 6d presents the time profiles of ln Co/C under illumination, where C is the concentration of RhB dye at illumination time t and Co is the original concentration of the RhB dye. As shown in Table 1, the BFCe product had the highest rate constant of 0.00311 min^{-1} which was roughly twice as large as that of the other prepared samples. Thus, the co-doping of F^{-} and Ce^{3+} resulted in a synergistic effect, thereby intensifying the photocatalytic performance (Li et al. 2018; Prasad et al. 2020).

The relationship between the rates of photodegradation and the surface area was investigated; Fig. 6e shows that the rate constant k was strictly related to the BET surface area of the photocatalytic materials and thus to the extent of RhB adsorption on the photocatalysts (Hou et al. 2012; Ahmed et al. 2020). The specific surface area and kinetic constants of the BVO were clearly minor. The larger surface areas and rate constant of BFCe appear to play a role in its photodecomposition rate

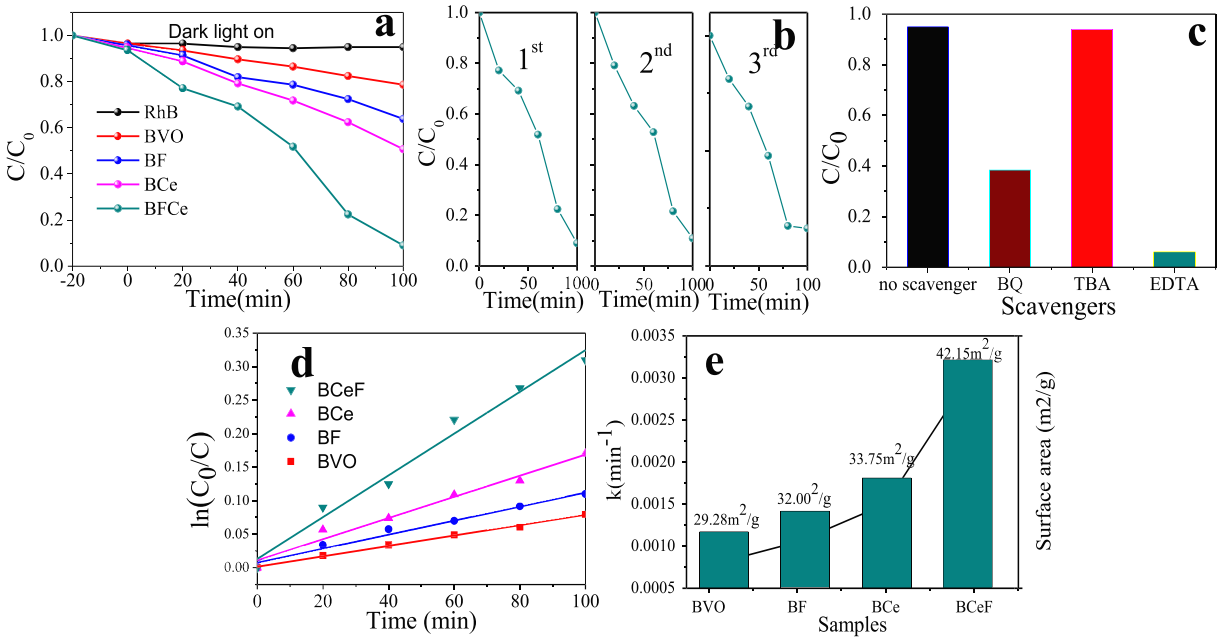

Fig. 6 **a** Photodegradation curves of RhB used as samples. **b** Recycling test for the photodegradation of RhB on BFCe. **c** Photocatalytic degradation of RhB over BFCe with the addition of BQ, TBA and EDTA. **d** Kinetics of the RhB degradation catalysed by as-products. **e** The kinetics rate constants (k) of photodegradation and surface areas of as-powdered under the visible light

which was higher than those of the BF and BCe samples (Zhao et al. 2019). The tendency between the BET surface area and the *D* from X-ray analyses was well corresponded due to the reduced agglomeration of the $BiVO_4$ particles. All these finding inferred that morphology and surface area were important for the photodegradation process.

Based on the above analyses, F^- and Ce^{3+} played a significant role on the photocatalytic performance of the co-doped BVO samples. The mechanism of the BFCe photoreaction is proposed in Fig. 6S to understand the role of F^- and Ce^{3+}. First, F^- and Ce^{3+} dopants resulted in lattice distortions because they entered into the pure $BiVO_4$ and substituted O^{2-} and Bi^{3+} locations, generating impurity energy levels in bismuth vanadate. These energy levels can trap the e^-, thereby enhancing the charge carrier separation efficiency and leaving more h^+ to share in the oxidation reactions. Second, F^- and Ce^{3+} co-doping prevented crystal phase change lead to formation of double-sided micro/nanostructure morphology, suitable V^{4+}/V^{5+} ratio and optimized energy band structures. Third, synergistic effects of F^- and Ce^{3+} may be responsible for an increased population of conductive e^- in the BFCe and efficient charge transport. As the main active species in degradation, the $\bullet O_2^-$ in the conduction band with more negative potentials is more appropriate for the decomposition of organic pollutants to small molecules. BFCe showed the most important photocatalytic performance, making it a good candidate compound for the application of organic contamination decomposition.

Conclusion

The experimental results illustrated that BFCe had the highest photocatalytic among the samples. The enhanced photocatalytic activity of BFCe indicated that the synergistic F^- and Ce^{3+} function as h^+ traps, thereby facilitating the separation of h^+ and e^-. To the best of our knowledge, a double-sided comb-like monoclinic $BiVO_4$ has not been reported previously. This type of monoclinic $BiVO_4$ with a new morphology and co-doped with F^- and Ce^{3+} is expected to expand its potential photocatalytic properties in environmental remediation and water splitting applications.

Compliance with ethical standards

Conflict of interest The authors declare that they have no conflict of interest.

References

Abbood HA, Huang K (2018) Photocatalysis of several organic dyes by a hierarchical Ag 2 V 4 O 11 micro – nanostructures. J Mater Sci Mater Electron 0:0 29:8068–8077. https://doi.org/10.1007/s10854-018-8813-x

Abbood HA, Peng H, Gao X et al (2012) Fabrication of cross-like NH4V4O10 nanobelt array controlled by CMC as soft template and photocatalytic activity of its calcinated product. Chem Eng J 209:245–254. https://doi.org/10.1016/j.cej.2012.08.027

Abbood HA, Ahmed KAM, Ren Y, Huang K (2013) MnV2O6×V2O5 cross-like nanobelt arrays: synthesis, characterization and photocatalytic properties. Appl Phys A Mater Sci Process 112:901–909. https://doi.org/10.1007/s00339-012-7444-y

Ahmed T, Ammar M, Saleem A et al (2020) Z-scheme 2D-m-BiVO 4 networks decorated by a g-CN nanosheet heterostructured photocatalyst with an excellent response to visible light. RSC Adv 10:3192–3202

Chen F, Yang Q, Yao F et al (2019) Synergetic transformations of multiple pollutants driven by BiVO 4 -catalyzed sulfite under visible light irradiation: reaction kinetics and intrinsic mechanism. Chem Eng J 355:624–636. https://doi.org/10.1016/j.cej.2018.08.182

Geng Y, Zhang P, Li N, Sun Z (2015) Synthesis of co doped BiVO<inf>4</inf> with enhanced visible-light photocatalytic activities. J Alloys Compd 651:744–748. https://doi.org/10.1016/j.jallcom.2015.08.123

Gu S, Li W, Wang F et al (2015) Synthesis of buckhorn-like BiVO4 with a shell of CeOx nanodots: effect of heterojunction structure on the enhancement of photocatalytic activity. Appl Catal B Environ 170–171:186–194. https://doi.org/10.1016/j.apcatb.2015.01.044

Gu S, Li W, Wang F, Li H, Zhou H (2016) Lanthanide ions Ce(III, IV) substituted for Bi in BiVO4 and its enhanced impact on visible light-driven photocatalytic activities. Catal Sci Technol 6:1870–1881

He B, Li Z, Zhao D et al (2018) Fabrication of porous Cu-doped BiVO 4 nanotubes as efficient oxygen-evolving photocatalysts. ACS Appl Nano Mater 1:2589–2599. https://doi.org/10.1021/acsanm.8b00281

Hoffmann MR, Martin ST, Choi W, Bahnemann DW (1995) Environmental applications of semiconductor photocatalysis. Chem Rev 95:69–96

Hou L, Yang L, Li J et al (2012) Efficient sunlight-induced methylene blue removal over one-dimensional mesoporous monoclinic BiVO4 nanorods. J Anal Methods Chem 345247:9. https://doi.org/10.1155/2012/345247

Hu J, He H, Li L, Zhou X, Li Z, Shen Q, Wu C, Asiri AM, Zhou Y, Zou Z (2019) Highly symmetrical, 24-faceted, concave $BiVO_4$ polyhedron bounded by multiple high-index facets for prominent photocatalytic O_2 evolution under visible light. Chem Commun 55:4777–4780. https://doi.org/10.1039/C9CC01366K

Huang ZF, Pan L, Zou JJ, Zhang X, Wang L (2014) Nanostructured bismuth vanadate-based materials for solar-energy-driven water oxidation: a review on recent progress. Nanoscale 6:14044–14063. https://doi.org/10.1039/c4nr05245e

Jaihindh DP, Thirumalraj B, Chen SM et al (2019) Facile synthesis of hierarchically nanostructured bismuth vanadate: an efficient photocatalyst for degradation and detection of hexavalent chromium. J Hazard Mater:647–657. https://doi.org/10.1016/j.jhazmat.2019.01.017

Jiang Z, Liu Y, Jing T et al (2016) Enhancing the photocatalytic activity of BiVO4 for oxygen evolution by Ce doping: Ce3+ ions as hole traps. J Phys Chem C 120:2058–2063. https://doi.org/10.1021/acs.jpcc.5b10856

Kim TW, Choi KS (2014) Nanoporous BiVO4photoanodes with dual-layer oxygen evolution catalysts for solar water splitting. Science. https://doi.org/10.1126/science.1246913

Kong D, Qi J, Liu D et al (2019) Ni-doped BiVO 4 with V 4+ species and oxygen vacancies for efficient photoelectrochemical water splitting. Trans Tianjin Univ 25:340–347

Kudo A, Ueda K, Kato H, Mikami I (1998) Photocatalytic O 2 evolution under visible light irradiation on BiVO 4 in aqueous AgNO 3 solution. Catal Lett 53:229–230

Lao JY, Huang JY, Wang DZ, Ren ZF (2004) Hierarchical oxide nanostructures. J Mater Chem:770–773. https://doi.org/10.1039/b311639e

Li JQ, Guo ZY, Liu H et al (2013) Two-step hydrothermal process for synthesis of F-doped BiVO4 spheres with enhanced photocatalytic activity. J Alloys Compd 581:40–45. https://doi.org/10.1016/j.jallcom.2013.06.141

Li W, Gao S, Li L, Jiao S, Li H, Wang J, Yu Q, Zhang Y, Wang D, Zhao L (2016) Hydrothermal synthesis of a 3D double-sided comb-like ZnO nanostructure and its growth mechanism analysis. Chem Commun 52:8231–8234. https://doi.org/10.1039/c6cc02072k

Li HB, Zhang J, Huang GY et al (2017) Hydrothermal synthesis and enhanced photocatalytic activity of hierarchical flower-like Fe-doped BiVO4. Trans Nonferrous Metals Soc China 27:868–875. https://doi.org/10.1016/S1003-6326(17)60102-X

Li Z, Jin C, Wang M (2018) Fabrication of Co3+ and B co-doping BiVO4 with improved photocatalytic performance for organic degradation. In: MATEC web of conferences. EDP Sciences, p 3008

Lin F, Shao Z, Li P et al (2017) Low-cost dual cocatalysts BiVO4 for highly efficient visible photocatalytic oxidation. RSC Adv 7:15053–15059. https://doi.org/10.1039/c6ra27559a

Liu AT, Tan G, Zhao C, et al (2017a) Enhanced photocatalytic mechanism of the Nd-Er co-doped tetragonal BiVO4 photocatalysts. https://doi.org/10.1016/j.apcatb.2017.05.018

Liu T, Tan G, Zhao C et al (2017b) Enhanced photocatalytic mechanism of the Nd-Er co-doped tetragonal BiVO 4 photocatalysts. Appl Catal B Environ 213:87–96. https://doi.org/10.1016/j.apcatb.2017.05.018

Lopes OF, Carvalho KTG, Nogueira AE et al (2016) Controlled synthesis of BiVO4 photocatalysts: evidence of the role of heterojunctions in their catalytic performance driven by visible-light. Appl Catal B Environ 188:87–97. https://doi.org/10.1016/j.apcatb.2016.01.065

Luo XL, Liu CJ, Chen MJ et al (2017) Electrochemical performance and enhanced photocatalytic activity of Ce-doped BiVO4under visible light irradiation. Mater Res Bull 94:428–434. https://doi.org/10.1016/j.materresbull.2017.06.042

Meng X, Zhang Z (2016) Bismuth-based photocatalytic semiconductors: introduction, challenges and possible approaches. J

Mol Catal A Chem 423:533–549. https://doi.org/10.1016/j.molcata.2016.07.030

Mohamed NA, Ullah H, Safaei J et al (2019) Efficient photoelectrochemical performance of gamma irradiated g-C3N4 and its g-C3N4@BiVO4 heterojunction for solar water splitting. J Phys Chem C. https://doi.org/10.1021/acs.jpcc.9b00217

Obregón S, Colón G (2014) Excellent photocatalytic activity of Yb3+, Er3+ co-doped BiVO4 photocatalyst. Appl Catal B Environ 152–153:328–334. https://doi.org/10.1016/j.apcatb.2014.01.054

Park HS, Kweon KE, Ye H et al (2011) Factors in the metal doping of BiVO4 for improved photoelectrocatalytic activity as studied by scanning electrochemical microscopy and first-principles density-functional calculation. J Phys Chem C 115:17870–17879

Park Y, McDonald KJ, Choi KS (2013) Progress in bismuth vanadate photoanodes for use in solar water oxidation. Chem Soc Rev 42:2321–2337. https://doi.org/10.1039/c2cs35260e

Pattengale B, Huang J (2016) The effect of Mo doping on the charge separation dynamics and photocurrent performance of BiVO4 photoanodes. Phys Chem Chem Phys 18:32820–32825. https://doi.org/10.1039/c6cp06407h

Pi Y, Liu M, Sun J et al (2014) Shape-controlled synthesis of BiVO4 hierarchical structures with unique natural-sunlight-driven photocatalytic activity. Appl Catal B Environ 152–153:413–424. https://doi.org/10.1016/j.apcatb.2014.01.059

Prasad U, Prakash J, Kannan A (2020) Effect of yttrium, ytterbium with tungsten co-doping on light absorption and charge transport properties of bismuth vanadate photoanodes to achieve superior photoelectrochemical water splitting. Sustainable Energy & Fuels

Regmi C, Kshetri YK, Ray SK et al (2017) Utilization of visible to NIR light energy by Yb +3 , Er +3 and Tm +3 doped BiVO 4 for the photocatalytic degradation of methylene blue. Appl Surf Sci 392:61–70. https://doi.org/10.1016/j.apsusc.2016.09.024

Regmi C, Kshetri YK, Pandey RP, Lee SW (2018) Visible-light-driven S and W co-doped dendritic BiVO4 for efficient photocatalytic degradation of naproxen and its mechanistic analysis. Mol Catal 453:149–160. https://doi.org/10.1016/j.mcat.2018.05.008

Regmi C, Kshetri YK, Kim TH et al (2019) Mechanistic understanding of enhanced photocatalytic activity of N-doped BiVO 4 towards degradation of ibuprofen: an experimental and theoretical approach. Mol Catal 470:8–18. https://doi.org/10.1016/j.mcat.2019.03.014

Saison T, Chemin N, Chanéac C et al (2015) New insights into BiVO<inf>4</inf> properties as visible light photocatalyst. J Phys Chem C 119:12967–12977. https://doi.org/10.1021/acs.jpcc.5b01468

Saithathul Fathimah S, Prabhakar Rao P, James V, Raj AK, Chitradevi GR, Leela S (2014) Probing structural variation and multifunctionality in niobium doped bismuth vanadate materials. Dalton Trans 43:15851–15860. https://doi.org/10.1039/c4dt01788a

Takashima T, Moriyama N, Fujishiro Y et al (2019) Visible-light-induced water splitting on hierarchically constructed Z-scheme photocatalyst composed of zinc rhodium oxide and bismuth vanadate. J Mater Chem A. https://doi.org/10.1039/C8TA12316K

Tan HL, Amal R, Ng YH (2017) Alternative strategies in improving the photocatalytic and photoelectrochemical activities of visible light-driven BiVO4: a review. J Mater Chem A 5:16498–16521. https://doi.org/10.1039/c7ta04441k

Tian X, Pei F, Fei J et al (2006) Synthesis and growth mechanism: a novel comb-like ZnO nanostructure. Phys E Low-Dimensional Syst Nanostruct 31:213–217. https://doi.org/10.1016/j.physe.2005.12.164

Ullah H, Tahir AA, Mallick TK (2018) Structural and electronic properties of oxygen defective and Se-doped p-type BiVO4(001) thin film for the applications of photocatalysis. Appl Catal B Environ 224:895–903. https://doi.org/10.1016/j.apcatb.2017.11.034

Usai S, Obregón S, Becerro AI, Colón G (2013) Monoclinic-tetragonal heterostructured BiVO4 by yttrium doping with improved photocatalytic activity. J Phys Chem C 117:24479–24484. https://doi.org/10.1021/jp409170y

Walsh A, Yan Y, Huda MN et al (2009) Band edge electronic structure of \ce{BiVO4}: elucidating the role of the bi \textit{s} and V \textit{d} orbitals. Chem Mater 21:547–551

Wang Q, Li Y, Zeng Z, Pang S (2012) Relationship between crystal structure and luminescent properties of novel red emissive BiVO 4:Eu 3+ and its photocatalytic performance. J Nanopart Res 14:1–8. https://doi.org/10.1007/s11051-012-1076-1

Wang M, Che Y, Niu C, Dang M, Dong D (2013a) Effective visible light-active boron and europium co-doped BiVO4 synthesized by sol-gel method for photodegradion of methyl orange. J Hazard Mater 262:447–455. https://doi.org/10.1016/j.jhazmat.2013.08.063

Wang M, Che Y, Niu C et al (2013b) Lanthanum and boron co-doped BiVO4 with enhanced visible light photocatalytic activity for degradation of methyl orange. J Rare Earths 31:878–884. https://doi.org/10.1016/S1002-0721(12)60373-1

Wang M, Niu C, Liu Q et al (2014) Enhanced photo-degradation methyl orange by N-F co-doped BiVO4 synthesized by sol-gel method. Mater Sci Semicond Process 25:271–278. https://doi.org/10.1016/j.mssp.2013.12.031

Wang M, Niu C, Liu J et al (2015) Effective visible light-active nitrogen and samarium co-doped BiVO<inf>4</inf> for the degradation of organic pollutants. J Alloys Compd 648:1109–1115. https://doi.org/10.1016/j.jallcom.2015.05.115

Wang B, Guo L, He T (2016) Fabrication of an olive-like BiVO 4 hierarchical architecture with enhanced visible-light photocatalytic activity. RSC Adv 6:30115–30124. https://doi.org/10.1039/c5ra21687g

Wang M, Guo P, Chai T et al (2017) Effects of Cu dopants on the structures and photocatalytic performance of cocoon-like Cu-BiVO4prepared via ethylene glycol solvothermal method. J Alloys Compd 691:8–14. https://doi.org/10.1016/j.jallcom.2016.08.198

Wang Z, Huang X, Wang X (2019) Highlights SC. Catal Today. https://doi.org/10.1016/j.cattod.2019.01.067

Xiao B, Lin L, Hong J, et al (2017) RSC advances synthesis of a monoclinic BiVO 4 nanorod array as the photocatalyst for efficient photoelectrochemical water oxidation. 7547–7554. https://doi.org/10.1039/c6ra28262h

Xu J, Bian Z, Xin X et al (2018) Size dependence of nanosheet BiVO4 with oxygen vacancies and exposed {0 0 1} facets on

the photodegradation of oxytetracycline. Chem Eng J 337: 684–696. https://doi.org/10.1016/j.cej.2017.12.133

Xue S, He H, Wu Z et al (2017) An interesting Eu,F-codoped BiVO4microsphere with enhanced photocatalytic performance. J Alloys Compd 694:989–997. https://doi.org/10.1016/j.jallcom.2016.10.146

Yang K, Li X, Yu C et al (2019) Review on heterophase/homophase junctions for efficient photocatalysis: the case of phase transition construction. Chin J Catal 40:796–818. https://doi.org/10.1016/S1872-2067(19)63290-0

Yin C, Zhu S, Chen Z et al (2013) One step fabrication of C-doped BiVO4 with hierarchical structures for a high-performance photocatalyst under visible light irradiation. J Mater Chem A 1:8367–8378. https://doi.org/10.1039/c3ta11833a

Yu C, He H, Liu X et al (2019) Novel SiO2 nanoparticle-decorated BiOCl nanosheets exhibiting high photocatalytic performances for the removal of organic pollutants. Chin J Catal 40:1212–1221. https://doi.org/10.1016/S1872-2067(19)63359-0

Zhang Y, Shi L, Geng Z et al (2019) The improvement of photocatalysis O 2 production over BiVO 4 with amorphous FeOOH shell modification. Sci Rep 9:1–10

Zhao Z, Luo W, Li Z, Zou Z (2010) Density functional theory study of doping effects in monoclinic clinobisvanite BiVO4 4. Phys Lett Sect A Gen Atomic Solid State Phys 374:4919–4927. https://doi.org/10.1016/j.physleta.2010.10.014

Zhao Y, Huang X, Gao F, Zhang L, Tian Q, Fang ZB, Liu P (2019) Study on water splitting characteristics of CdS nanosheets driven by the coupling effect between photocatalysis and piezoelectricity. Nanoscale 11:9085–9090. https://doi.org/10.1039/c9nr01676g

Zheng J, Xiong FQ, Zou M et al (2016) Enhanced photocatalytic degradation of rhodamine B under visible light irradiation on mesoporous anatase TiO 2 microspheres by codoping with W and N. Solid State Sci 54:49–53. https://doi.org/10.1016/j.solidstatesciences.2015.10.008